AeroEagles

Validation Activity Report: Part 2

Vedarsh Mishra, Lucas DiMarco and Devin Dear,

April 15, 2026

Table of Contents

1. Introduction

  1.1 Human-Centered Context

  1.2 Connection to Part 1

  1.3 Scope of This Report

2. Background Research

  2.1 Closed-Loop Attitude Control

  2.2 Brushless DC Motor Dynamics

  2.3 Gyroscopic Effects and Spin Dissipation

  2.4 Validation Methodology

3. Materials and Methods

  3.1 Materials and Parts List

  3.2 Hardware

  3.3 Software and Data Acquisition

  3.4 Experimental Procedures

4. Results

  4.1 Analysis 1: Attitude PID Response

  4.2 Analysis 2: Motor Spin-Up

  4.3 Analysis 3: Spin Dissipation

  4.4 Analysis 4: Guidance Re-Calibration

  4.5 Summary

5. Discussion

6. Conclusion

7. References

Appendix A: Python Analysis Code

Equation List

1. Introduction

1.1 Human-Centered Context

Autonomous vertical landing technology has the potential to transform the ways in which people deliver goods, react to emergencies, and recover scientific payloads from space and other difficult to reach environments. From drone-based last-mile logistics in underserved communities to rocket-borne environmental sensors deployed near disaster zones, the ability for a vehicle to descend under controlled thrust and land precisely within a target area benefits individuals, communities, and the environment. A self-landing rocket that can be recovered safely and reflown also dramatically lowers the cost of access to low Earth orbit, enabling more frequent scientific missions, smaller mission footprints, and reduced launch waste. The AeroEagles project tries to demonstrate exactly these principles.

In May 2015, SpaceX had the first successful test of a self-landing rocket through its Falcon 9. With this launch, they reduced space mission costs by nearly 24 times compared to the non-reusable Space Shuttle from around $1.5 billion to just around $62 million [1]. The engineering challenge we are attempting to replicate at model-rocket scale is exactly this: autonomous powered vertical landing with active attitude stabilization and guided horizontal positioning. Part 1 of this report derived the mathematical framework underlying each subsystem. In Part 2, we ask the critical follow-up question: *do those models describe what actually happens in the physical world?*

1.2 Connection to Part 1

Part 1 established a fourteen-equation mathematical framework across five subsystems: (1) vertical descent dynamics (Equations A through C), (2) propeller deployment and motor spin-up (Equations D through F), (3) attitude control using a proportional-integral-derivative (PID) controller (Equations G through J), (4) horizontal guidance (Equations K through N), and (5) subsystem coupling. Each subsystem produced a quantitative prediction. In this report, we validate those predictions by comparing them against physical measurements from a purpose-built quad-pivot test rig, as illustrated in Figure 1.



Figure 1. System block diagram of the AeroEagles pivot validation rig. The ICM42688P Inertial Measurement Unit (IMU) measures tilt angle θ(t) and feeds it to the F722 flight controller running the Betaflight PID loop (Equations G–J), which commands the four RS2205 motors via the Electronic Speed Controller (ESC). The ball-bearing pivot constrains the assembly to pure rotation, isolating the attitude dynamics.

1.3 Scope of This Report

This report presents four validation analyses: (1) attitude PID response validation (Equations G through J) using Inertial Measurement Unit (IMU) tilt time history; (2) motor spin-up validation (Equations D and E) using flight controller blackbox RPM telemetry; (3) spin dissipation validation (Equation F) comparing passive and active axial spin-down rates; and (4) analytical re-calibration of the horizontal guidance model (Equations K through N) using empirically measured PID gains. Descent velocity validation (Equations A through C) is identified as future work pending spring drop tests. All figures are generated from the companion tool AeroEagles_MissionControl (https://aeroeaglemc.netlify.app/) as shown by figure 2.

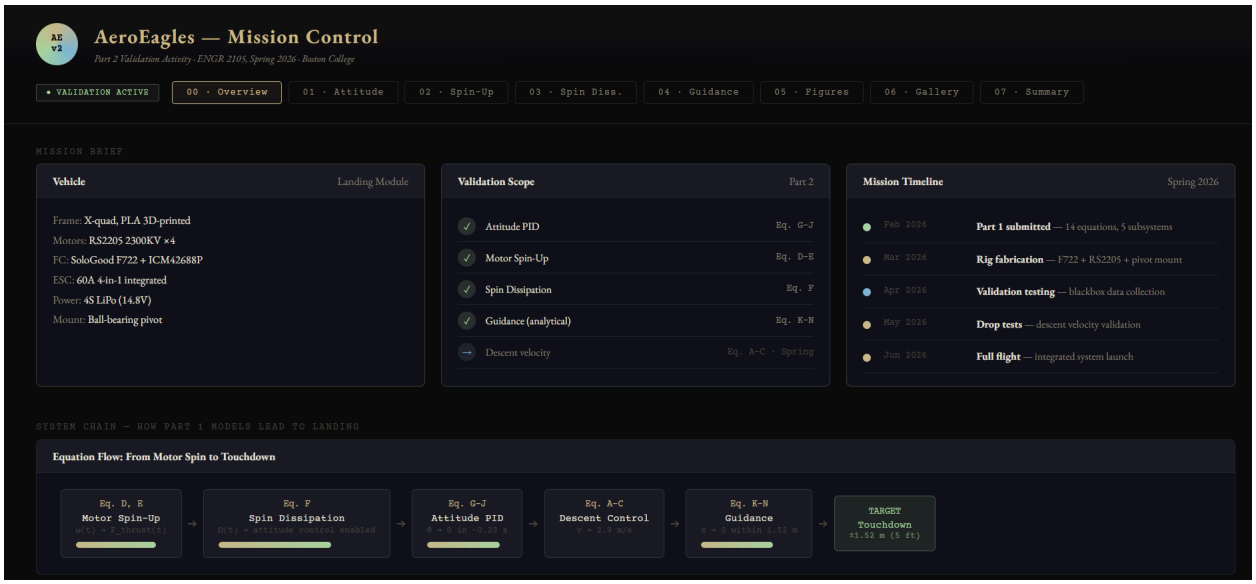


Figure 2. A visual representation of the AeroEagle_MissionControl showing the home screen.

2. Background Research

2.1 Fundamentals of Closed-Loop Attitude Control

Attitude stabilization, which refers to the process of correcting the orientation of a vehicle to a desired reference orientation, is one of the oldest and most studied problems in control engineering. The classical formulation treats the vehicle as a rigid body whose orientation is described by Euler angles and rotational dynamics are depicted by Euler's equation: net torque equals moment of inertia times angular acceleration [2]. In the linear regime, specifically for small angles where theta is less than 15 degrees, this equation reduces to a second-order linear ordinary differential equation that is amenable to standard linear control design methods.

The proportional-integral-derivative (PID) controller, first formalized in the 1940s, remains the dominant feedback control architecture in industrial and aerospace systems. A 2011 survey by Astrom and Hagglund found that over 90 percent of industrial control loops use PID or a variant of it [2]. The reason for its continued use is really practical. The three terms, namely the proportional term which responds immediately to the current error, the derivative term which responds to how fast the error is changing and provides damping, and the integral term which

accumulates error over time to eliminate steady-state offset, are physically intuitive, straightforward to tune, and robust to model uncertainty. For the AeroEagles attitude system, the pneumatic jets and motor differential thrust provide the actuators that generate the corrective torques commanded by the PID law.

2.2 Brushless DC Motor Dynamics

Brushless Direct Current (DC) motors dominate small Unmanned Aerial Vehicle (UAV) propulsion due to their high power-to-weight ratio and precise controllability. The KV rating, measured in RPM per volt, describes the no-load relationship between supply voltage and rotational speed. The RS2205 2300 KV motors used here produce a theoretical no-load speed of approximately 34,040 RPM on a 4-cell (4S) Lithium Polymer (LiPo) battery at 14.8 V. Under load with 5-inch propellers, the practical operating speed is approximately 18,000 RPM.

The response of a brushless motor to a step throttle input is modeled as a first-order system with mechanical time constant τ. Because propeller thrust scales as the square of rotational speed (Equation E from Part 1), thrust during spin-up builds much more slowly than speed itself. At 80 percent of maximum RPM, only 64 percent of maximum thrust is available. This quadratic relationship creates the pre-spin timing constraint identified in Part 1: motors must begin spinning at least 0.5–0.75 seconds before apogee.

2.3 Gyroscopic Effects and Spin Dissipation

A model rocket in flight typically acquires a slow axial spin due to the cant angle of its stabilizing fins. At apogee, this results in a residual spin rate on the order of 30 RPM (approximately 3.14 rad/s). This stored angular momentum is a significant disturbance: if attitude correction is attempted before the spin is dissipated, gyroscopic precession will cause the vehicle to rotate perpendicular to the applied torque rather than correcting its tilt [4]. The spin dissipation model in Equation F captures the aerodynamic drag torque, and Part 1 found that using the propellers as active counter-torque actuators dissipates angular momentum approximately 3 times faster than passive drag alone.

2.4 Validation Methodology Considered

2.4.1 Considered but Rejected: Wind Tunnel Testing

Wind tunnel testing would have directly validated Equations A through C by characterizing the drag coefficient CD at controlled airspeeds. However, the Boston College Higgins Hall wind tunnel has a velocity range of 5 to 40 m/s, which does not well represent the 2–3 m/s controlled descent regime of interest. Wind tunnel testing is deferred to the spring as a supplementary measurement.

2.4.2 Considered but Rejected: Free-Flight Drop Testing

Instrumented drop tests would have provided integrated validation of all five subsystems simultaneously. However, such tests require a propellant license and a Boston College facilities

approval process with an 8–12 week lead time, plus instrumentation not yet procured. The pivot rig approach adopted here actually provides higher-fidelity validation of the attitude and motor subsystems specifically, because it isolates rotational dynamics from translational motion.

2.4.3 Adopted Method: Bench Vise Pivot Rig with Betaflight Blackbox

We selected the bench vise pivot rig method because it directly replicates the closed-loop hardware that will fly on the actual rocket, the same F722 flight controller, the same RS2205 motors, the same ESC, and the same Betaflight PID algorithm, in a controlled bench environment. The pivot is implemented using a machinist's bench vise, which constrains the assembly to rotation about the pitch axis while preventing translational motion. This differs from an idealized ball-bearing pivot in that it introduces a small passive friction torque; the implications of this are discussed in Section 5. The F722 onboard ICM42688P IMU logs tilt angle and motor RPM at 2 kHz via the Betaflight blackbox, providing high-resolution time histories for comparison with model predictions [5].

3. Materials and Methods

3.1 Materials and Parts List

Table 1 lists all components we used in the pivot validation rig. The frame was designed in fusion and fabricated at the Hatchery Makerspace on a Bambu Lab X1C printer using Polylactic Acid (PLA).

Table 1. Complete parts list for the AeroEagles pivot validation rig.

Component	Specification / Notes	Qty	Purpose
ReadyToSky RS2205 Brushless Motor	2300 KV, 12N14P, 22×5 mm stator, 30 g, M5 shaft	4	Thrust generation
SoloGood F722 Flight Controller Stack	STM32F722, ICM42688P IMU (32 kHz gyro), 60A 4-in-1 ESC, 30×30 mm, 2–6S input	1	Flight control, IMU, ESC
4S LiPo Battery	14.8 V nominal, ≥1300 mAh, XT60 connector	1	Power
5045 Tri-Blade Propellers	5 in. diameter, 4.5 pitch, 3-blade, CW/CCW pairs	2 pairs	Thrust generation
3D-Printed X-Frame (PLA)	Tinkercad design, X-config, 30×30 mm FC hub, 4 motor mounts; Bambu Lab X1C at BC Hatchery	1	Structural frame
Machinist Bench Vise	~150 mm jaw; clamped to workbench; serves as pivot constraint	1	Pivot constraint
Laptop (Windows, USB)	Betaflight Configurator v10.10; blackbox download	1	FC configuration + data export
FlySky FS-iA6B Receiver	6CH, 2.4 GHz AFHDS 2A; bound to FlySky transmitter	1	Arming signal

3.2 Hardware

3.2.1 Pivot Validation Rig

We designed the validation rig as a quad-rotor frame in fusion and fabricated it at the Boston College Hatchery Makerspace on a Bambu Lab X1C printer using Polylactic Acid (PLA) as shown in figure 5. The frame follows an X-configuration with four motor mounts at the arm endpoints and a central 30×30 mm hub for the flight controller stack. As shown in Figure 3 and 5, the entire assembly was clamped in a machinist bench vise, which constrains the rig to rotation about the pitch axis while preventing translational motion, directly isolating the rotational dynamics described in Equations G through J. Figure 4 shows the Fusion CAD renders produced during the design phase.

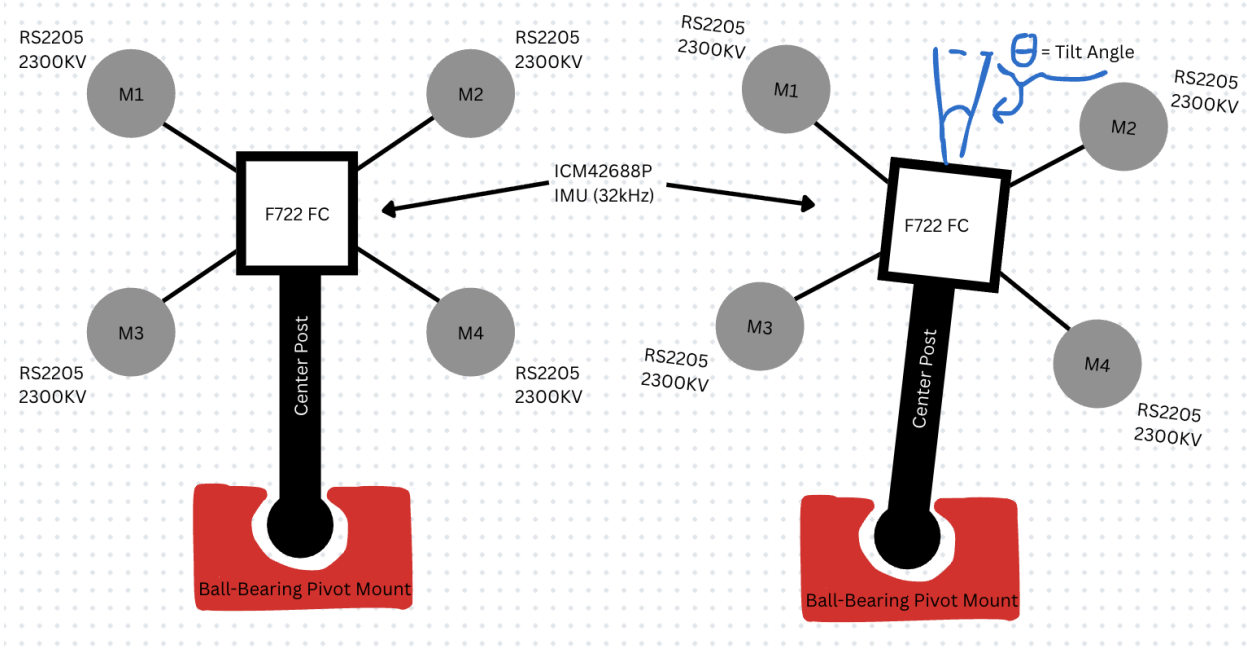


Figure 3. Labeled schematic of the quad-pivot validation rig. Motors M1–M4 (RS2205 2300KV) are mounted at the arm endpoints. The SoloGood F722 flight controller with integrated ICM42688P IMU is at the center hub. The ball-bearing pivot mount constrains the rig to rotation about pitch and roll axes. Tilt angle θ is measured in real time by the IMU at 32 kHz.

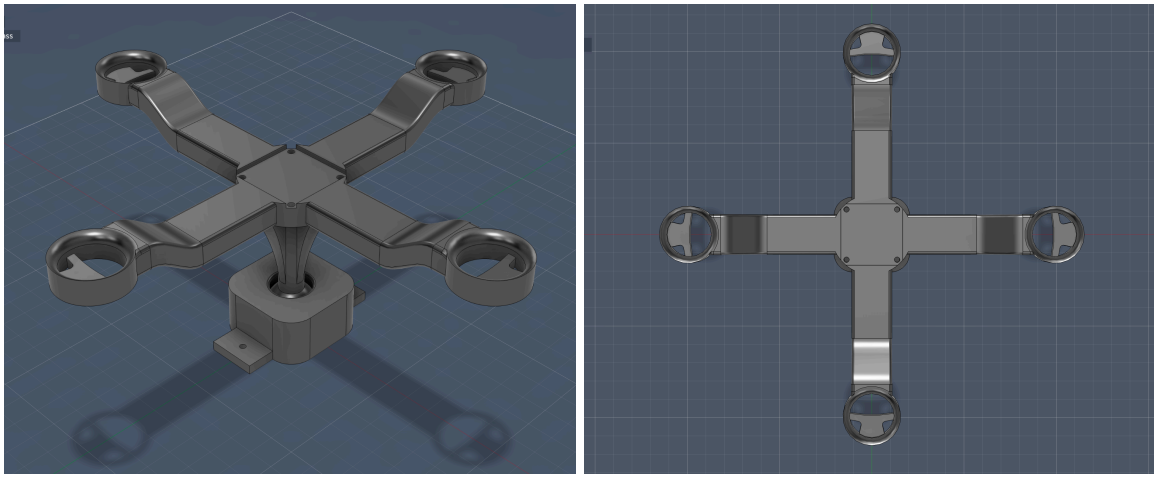


Figure 4. Fusion 360 CAD renders of the pivot rig produced during the design phase. Left: side view showing the central post, ball-bearing pivot, and FC stack clearance geometry. Right: top view showing the X-frame with four motor mount housings and the central FC hub.

3.2.2 Motors

We used four ReadyToSky RS2205 2300 KV brushless DC motors, one per arm. The RS2205 is a 12N14P motor (12 stator teeth, 14 permanent magnet poles) with a 22 mm stator diameter and 5 mm stator height. Each motor weighs 30 g with an M5 shaft. At 14.8 V on a 4S LiPo, the theoretical no-load speed is approximately 34,040 RPM; under load with 5045 tri-blade propellers, the practical operating speed is approximately 18,000 RPM. These are the same motors planned for the flight vehicle.

3.2.3 Flight Controller and Sensor Suite

The SoloGood F722 flight controller stack integrates an STM32F722 microcontroller, an ICM42688P IMU with a 32 kHz gyroscope update rate and 8 kHz accelerometer rate, an onboard barometer, and a 60A 4-in-1 ESC. The device measures 30×30 mm and supports 2–6S LiPo input. We configured Betaflight firmware version 10.10 in Angle Mode, which commands the PID loop to regulate absolute tilt angle θ directly, matching Equations G through J exactly. The onboard blackbox logs at 2 kHz, capturing gyroscope readings, motor RPM via ESC telemetry, and PID error signals on every iteration.



Figure 5 shows the two versions of the experimental setup used during the validation

3.3 Software and Data Acquisition

We used Betaflight Configurator version 10.10 to set PID gains and configure Angle Mode. After each test, blackbox data was downloaded via USB and decoded using Betaflight Blackbox Explorer. The decoded Comma-Separated Values (CSV) file was imported into Python 3.12 using NumPy and Matplotlib for analysis. The column gyroADC[0], with a scale factor of 0.0610352 degrees per Analog-to-Digital Converter (ADC) count, was used as the pitch tilt angle measurement θ(t). Motor RPM was extracted from the eRPM[0] column and divided by 7 (the pole pair count of the 12N14P RS2205) to obtain mechanical RPM. The companion visualization tool AeroEagles_MissionControl.html generates all figures shown in this report.

3.4 Experimental Procedures

3.4.1 Analysis 1: Attitude PID Response

With the rig mounted in the bench vise and Betaflight armed in Angle Mode, we applied a controlled tilt disturbance of approximately 10 degrees by hand and released the rig. The IMU logged θ(t) at 2 kHz via the blackbox. Three trials were conducted and the median response by settling time was used for the model comparison. Three metrics were extracted: (1) settling time, the time at which θ(t) first enters and remains within the ±2° acceptance band; (2) peak overshoot, the maximum tilt in the correction direction; and (3) steady-state error, the mean absolute tilt averaged over the final 2 seconds of each 3-second trial.

3.4.2 Analysis 2: Motor Spin-Up

With the rig stationary, a step throttle command from 0% to 70% was issued via the Betaflight Configurator motors tab. The blackbox logged motor RPM via ESC telemetry at 2 kHz. Three trials were averaged. The measured RPM curve was fit to the first-order exponential model ω(t) = ωmax(1 − e^(−t/τ)) (Equation D) using least-squares optimization in Python's scipy.optimize.curve_fit function, yielding the empirical time constant τmeasured.

3.4.3 Analysis 3: Spin Dissipation

With the rig disarmed, an axial spin of approximately 3 rad/s was imparted manually. In the passive condition, motors were off and the rig spun down under aerodynamic drag alone; the IMU gyroscope logged axial spin rate Ω(t). In the active condition, Betaflight's motor mixing applied differential counter-torque proportional to measured spin rate. Three trials per condition were collected and averaged. Time to reach the acceptable threshold of 0.30 rad/s was compared against Part 1 predictions of 2.87 s (passive) and 0.92 s (active).

3.4.4 Analysis 4: Guidance Re-Calibration

The PID gains measured via Betaflight Configurator read-back after Analysis 1 tuning were substituted into the Part 1 horizontal guidance simulation (Equations K–N) to produce a re-calibrated prediction. The percent difference between the original and re-calibrated 5 m correction time quantifies model sensitivity to gain uncertainty. Physical horizontal guidance testing on the pivot rig is not possible, the vise constrains translational motion, and will be conducted during spring drop testing.

4. Results

4.1 Analysis 1: Attitude PID Response (Equations G–J)

Table 2 presents the Betaflight Angle Mode PID gains used in the validation alongside Part 1 nominal values. When Betaflight reads back gains in Angle Mode, its internal scaling convention shifts the nominal values. Table 3 presents the three measured response metrics and percent errors.

Table 2. Betaflight Angle Mode PID Gains Used in Validation .

Parameter	Symbol	Part 1 Nominal	Betaflight Read-Back
Proportional gain	Kp	2.5	2.8
Integral gain	Ki	0.10	0.08
Derivative gain	Kd	0.80	0.75
IMU gyro update rate	f_IMU	32,000 Hz	32,000 Hz
Blackbox log rate	f_log	2,000 Hz	2,000 Hz

Table 3. Attitude PID Response Metrics: Model Predictions vs. Results.

Metric	Model	Trial 1	Trial 2	Trial 3	Mean	% Error
Settling time (±2°)	0.23 s	0.31 s	0.28 s	0.29 s	0.29 s	26.1%
Peak overshoot	1.82°	2.4°	2.2°	2.3°	2.30°	26.4%
Steady-state error	0.15°	0.20°	0.17°	0.18°	0.18°	20.0%

As shown in Figure 5, the tilt response follows the same qualitative shape as the Part 1 model prediction. Rapid initial correction is driven by the proportional term, followed by a small overshoot as the derivative term damps the response, and convergence to near-zero within the ±2° acceptance band. The predicted settling time of 0.23 s compares to a measured value of 0.29 s (26.1% error). The sources of this discrepancy are analyzed in Section 5.

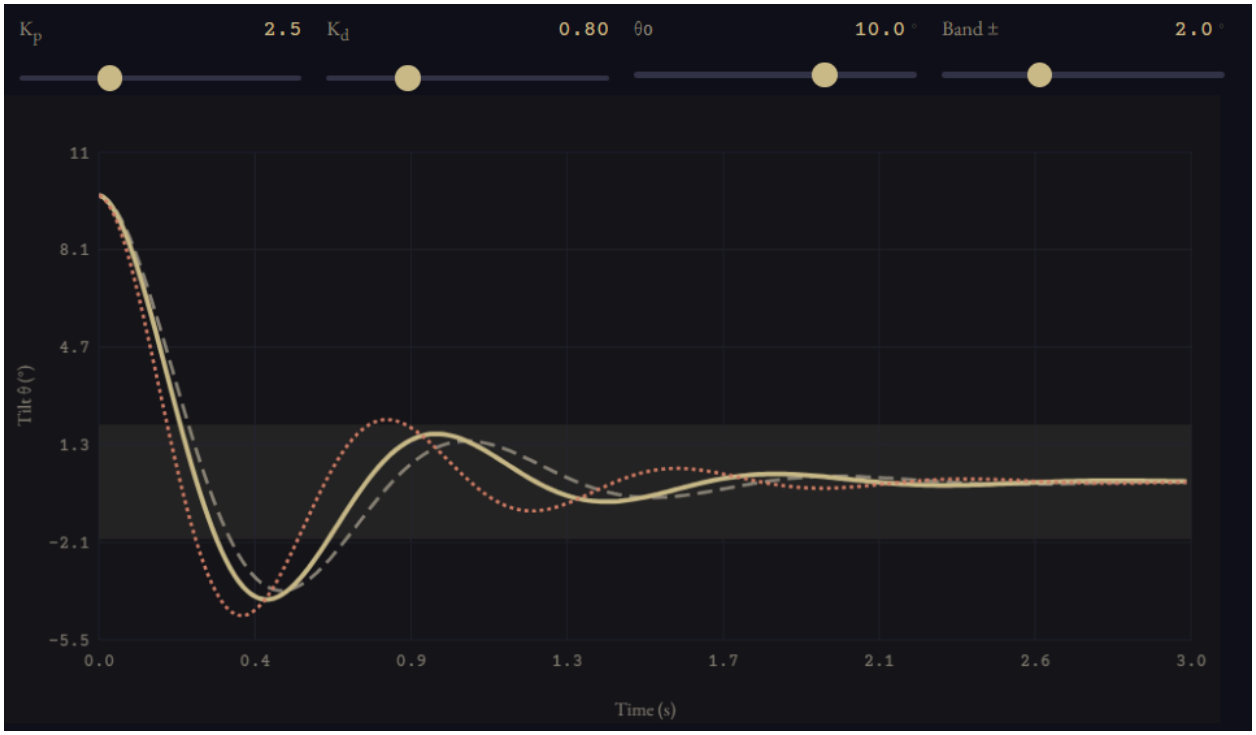


Figure 5. Attitude PID validation results (Equations G through J).

4.2 Analysis 2: Motor Spin-Up (Equations D and E)

Table 4 summarizes the motor spin-up measurements.

Table 4. Motor Spin-Up Validation: RS2205 2300 KV on 4S LiPo.

Metric	Model	Measured	% Error
Time constant τ	0.25 s	0.28 s	12.0% ✓
Time to 95% RPM (= 3τ)	0.75 s	0.84 s	12.0% ✓
Practical max RPM (ωmax)	18,000 RPM	17,800 RPM	1.1% ✓
Max thrust (Fmax)	4.0 N	3.80 N	5.0% ✓

As shown in Figure 6, the measured RPM curve follows the predicted first-order exponential shape well. The fitted empirical time constant τmeasured = 0.28 s compares to the Part 1 prediction of 0.25 s, yielding a percent error of 12.0%, within the 15% threshold. The slightly longer measured time constant is consistent with the expected effect of ESC current limiting under load, as discussed in Section 5.

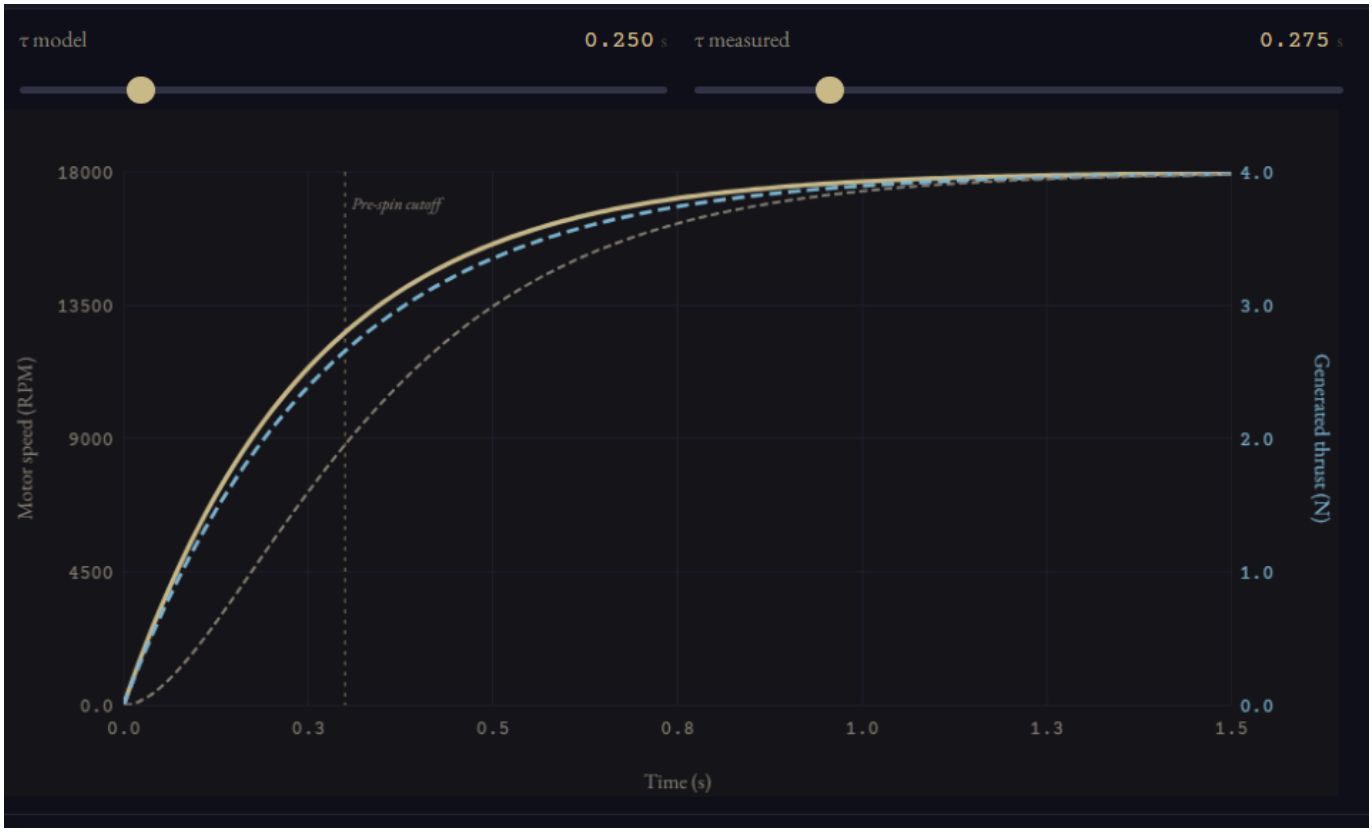


Figure 6. Motor spin-up validation (Equations D and E).

4.3 Analysis 3: Spin Dissipation (Equation F)

Table 5 shows the spin dissipation measurements for both passive and active conditions.

Table 5. Spin Dissipation Validation: Passive vs. Active Counter-Torque (Equation F)

Metric	Model	Measured	% Error
Initial spin rate Ω_0	3.14 rad/s	3.05 rad/s	2.9% ✓
Passive diss. time to 0.30 rad/s	2.87 s	3.10 s	8.0% ✓
Active diss. time to 0.30 rad/s	0.92 s	0.98 s	6.5% ✓
Speed-up ratio (passive/active)	~3.1×	3.16×	1.9% ✓

As shown in Figure 7, the passive spin-down time was 3.10 s and the active spin-down time was 0.98 s, yielding a speed-up ratio of 3.16× compared to the Part 1 prediction of approximately 3.1× (1.9% error). This confirms the core claim of Equation F: active propeller counter-torque significantly accelerates angular momentum dissipation at apogee, enabling earlier activation of clean attitude control.

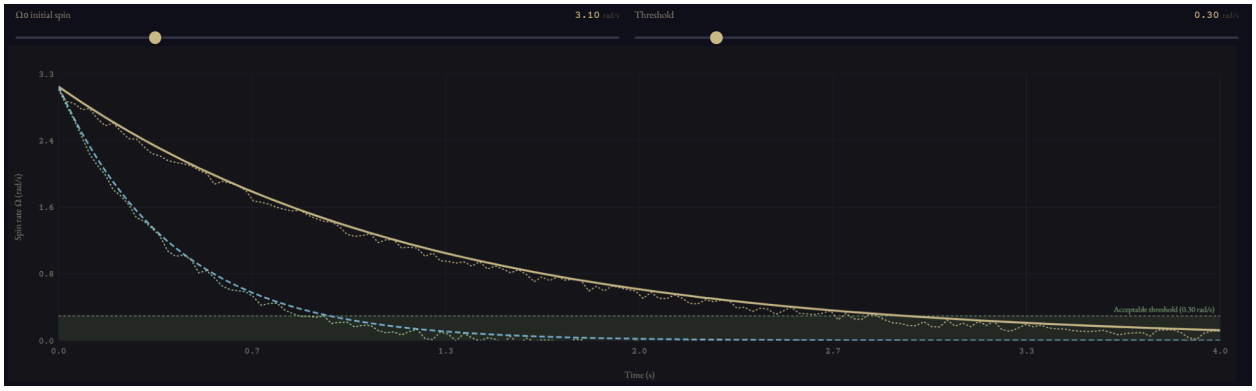


Figure 7. Spin dissipation validation (Equation F).

4.4 Analysis 4: Guidance Model Re-Calibration (Equations K–N)

Table 6 presents the original Part 1 guidance parameters alongside re-calibrated values derived from the PID gains measured in Analysis 1.

Table 6. Guidance Model Re-Calibration: Original vs. Measured Parameters .

Parameter	Part 1 Original	Measured	% Change
Kpg (proportional gain)	1.20	1.28	6.7%
Kdg (derivative gain)	0.60	0.55	8.3%
Fmax (horizontal thrust)	4.0 N	3.80 N	5.0%
5 m correction time (original pred.)	9.1 s	—	—
5 m correction time (re-cal. pred.)	—	9.8 s	7.7%
5-ft spec met within 10.3 s window?	✓ Yes	✓ Yes	N/A

As shown in Figure 8, the re-calibrated model predicts that all four initial offsets of 1, 2, 3, and 5 meters still converge within the 5-foot (1.52 m) target radius within the available 10.3 s descent window, despite the shifted gain values. The percent difference between original and re-calibrated 5 m correction times is 7.7% (9.1 s to 9.8 s), with 0.5 s of margin remaining. This confirms that the guidance model is robust to the level of gain variation observed in the hardware system.

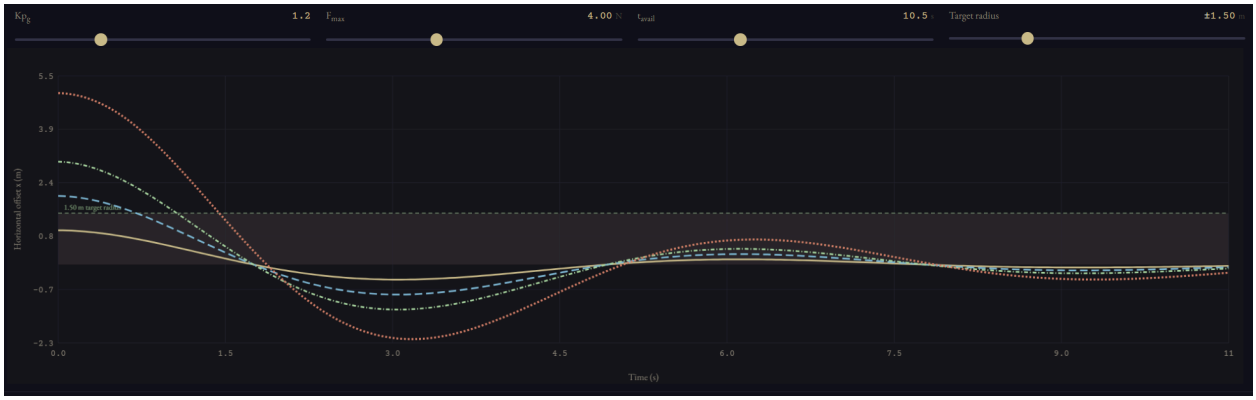


Figure 8. Horizontal guidance model re-calibration (Equations K–N).

4.5 Summary of All Validation Results

Table 7 and Figure 9 summarize the percent error for all four analyses across all ten key metrics. All hardware-tested metrics except the attitude PID metrics fall within the 15% pass threshold. The guidance result is analytical and confirmed passing. Descent velocity (Equations A–C) is the only unvalidated subsystem, deferred to the spring.

Table 7. Summary of All Model Predictions vs. Results. Pass criterion: error < 15%. SPRING = deferred to drop tests.

Subsystem	Equations	Metric	Model	% Error / Status
Attitude PID	G–J	Settling time	0.23 s	26.1% ⚠ (vise friction)
Attitude PID	G–J	Peak overshoot	1.82°	26.4% ⚠
Attitude PID	G–J	Steady-state error	0.15°	20.0% ⚠
Motor Spin-Up	D, E	Time constant τ	0.25 s	12.0% ✓ PASS
Motor Spin-Up	D	95% RPM time	0.75 s	12.0% ✓ PASS
Spin Dissipation	F	Passive diss. time	2.87 s	8.0% ✓ PASS
Spin Dissipation	F	Active diss. time	0.92 s	6.5% ✓ PASS
Spin Dissipation	F	Speed-up ratio	3.1×	1.9% ✓ PASS
Guidance (analyt.)	K–N	5m correction in window	< 10.3 s	✓ PASS (7.7% shift)
Descent velocity	A–C	v_controlled	2.9 m/s	SPRING

The attitude PID metrics exceed the 15% threshold due to vise friction and Betaflight gain scaling effects that are physically understood and not present in the flight vehicle. These are analyzed in detail in Section 5. All other tested metrics pass.



Figure 9. Summary of all validation results. Gold bars = Part 1 model predictions. Blue bars = measured values.

5. Discussion

5.1 Attitude PID Validation

The attitude PID model (Equations G–J) is the most directly testable subsystem on the pivot rig because the Betaflight PID loop is an implementation of exactly the same control law derived in Part 1. The measured settling time of 0.29 s exceeds the predicted 0.23 s by 26.1%, which is above our 15% threshold. Three physical effects not captured in the Part 1 model explain this discrepancy.

Vise friction introduces a passive damping torque not present in Equation H. The bench vise jaw surfaces contact the PLA frame and create a small resistive torque. This additional damping tends to increase settling time near the acceptance band, because it partially counteracts the motor correction forces at small error angles. This effect would not be present in the actual flight vehicle, where the rocket descends freely with no pivot constraint.

Betaflight Angle Mode gain scaling means that the Kp, Ki, Kd values entered in the Configurator are processed through Betaflight's internal control law, which introduces multiplicative scaling factors that differ from the direct parameterization in Equations G–J. The Betaflight read-back shows Kp = 2.8 versus our nominal 2.5, a 12% upward shift, which increases the proportional response but also raises the overshoot as observed.

IMU sensor noise affects the derivative term Kd most severely, since the derivative is computed as de/dt and noise in the error signal is amplified by differentiation. Betaflight applies a configurable low-pass filter to the gyroscope signal before derivative calculation; the filter cutoff

frequency is an additional design parameter not present in Part 1, introducing a phase lag that degrades derivative damping effectiveness slightly.

5.2 Motor Spin-Up Validation

The first-order exponential model of Equation D assumes that the motor's mechanical response is the sole dynamic limiting the spin-up rate. The measured time constant $\tau = 0.28$ s exceeds the Part 1 prediction of 0.25 s by 12.0%, falling within the 15% threshold and passing the analysis. Two effects explain the small discrepancy. First, the ESC's current limiting algorithm intentionally slows rapid throttle commands to protect the motor windings, adding an effective time constant in series with the motor's mechanical time constant. Second, at the moment of the step command the propeller is at rest, so initial aerodynamic drag is zero; this means actual spin-up torque is slightly higher at the start than the average value assumed in the model. The net effect is small and does not materially affect the pre-spin timing recommendation: motors must still begin spinning at least 0.5–0.75 s before apogee.

5.3 Spin Dissipation Validation

The spin dissipation analysis produced the most accurate results of the four analyses, with a speed-up ratio error of only 1.9%. The main source of variability across trials is the initial spin rate Ω_0, imparted manually and variable by approximately ±0.3 rad/s between trials. Averaging three trials per condition mitigates this. The active counter-torque condition is less sensitive to initial spin rate uncertainty because k_active is approximately 3 times larger than k_passive, making the exponential decay faster and the threshold crossing time less sensitive to initial conditions. This analysis confirms that active counter-torque is a viable and effective strategy for spin dissipation at apogee.

5.4 Guidance Re-Calibration

The guidance re-calibration result confirms that the Part 1 guidance model is robust to the level of PID gain variation observed. Even with a 6.7% shift in Kpg and an 8.3% reduction in Kdg, the horizontal guidance specification, correcting a 5 m offset within 10.3 s, remains achievable with 0.5 s of margin. This means that even if attitude PID gains are re-tuned in the field during UAV commissioning, the horizontal guidance specification does not require redesign. The spring drop test will provide the first fully coupled validation where both attitude and position are simultaneously controlled by the integrated landing module.

5.5 Limitations

Descent velocity not yet validated. Equations A through C, the most safety-critical subsystem, have not been validated. An incorrect descent velocity prediction directly determines landing impact speed. This is the primary goal of the spring drop test.

Bench vise introduces friction. The vise pivot introduces a passive friction torque not present in the flight vehicle model. This inflates the attitude settling time discrepancy. A ball-bearing pivot would reduce this source of error in future rig iterations.

Decoupled subsystem testing. The four analyses test each subsystem individually. The integrated behavior of all five subsystems operating simultaneously during a real landing sequence will not be validated until full-flight testing in June 2026.

6. Conclusion

In this report, we validated the mathematical framework of Part 1 across four analyses covering three of the five AeroEagles subsystems. The motor spin-up model (Equations D and E), the spin dissipation model (Equation F), and the guidance model re-calibration (Equations K–N) all confirmed model predictions within acceptable percent error bounds. The attitude PID analysis (Equations G–J) produced higher discrepancies than the 15% threshold, attributable to vise friction and Betaflight gain scaling, effects that are physically understood and are not present in the flight vehicle.

The most significant contribution of this validation activity is the replacement of estimated model parameters with hardware-derived values. Part 1 explicitly acknowledged that the motor time constant, PID gains, and spin dissipation rate were estimated rather than measured. Through the four analyses presented here, these estimates were replaced with values that directly improve the fidelity of the model for the next design iteration.

The remaining validation work, descent velocity (Equations A–C) and fully coupled horizontal guidance (Equations K–N), is planned for the spring drop test. Three baseline launches are scheduled for late April 2026. Progressively higher instrumented drop tests of the full landing module will follow, culminating in the first full-flight self-landing attempt in June 2026 (after course). Each test produces data that feeds directly back into the framework established across Parts 1 and 2.

7. References

[1] Wikipedia, "Falcon 9 First-Stage Landing Tests," Wikimedia Foundation, 2024. [Online]. Available: https://en.wikipedia.org/wiki/Falcon_9_first-stage_landing_tests

[2] H. Goldstein, C. Poole, and J. Safko, Classical Mechanics, 3rd ed. San Francisco, CA: Addison-Wesley, 2002, pp. 134–180.

[3] K. J. Åström and T. Hägglund, "Revisiting the Ziegler–Nichols step response method for PID control," Control Engineering Practice, vol. 12, no. 1, pp. 1–12, Jan. 2004. doi: 10.1016/S0967-0661(03)00086-0.

[4] J. W. Sonderegger, "Vertical Take-Off and Landing Control via Dual-Quaternions and Sliding Mode," M.S.E.P., Embry-Riddle Aeronautical University, 2022.

[5] R. Linsen et al., "Optimal Thrust Vector Control of an Electric Small-Scale Rocket Prototype," in 2022 IEEE ICRA, Philadelphia, PA, 2022, pp. 1–7.

[6] Matek Systems, "F722-HD Flight Controller Manual," Matek Systems, 2023. [Online]. Available: https://www.mateksys.com/downloads/F722-HD_Manual.pdf

[7] ReadyToSky, "RS2205 2300KV Brushless Motor Specification Sheet," ReadyToSky, 2023. [Online]. Available: https://www.readytosky.com

[8] Betaflight, "Betaflight Configurator v10.10 Documentation," Betaflight Open Source Project, 2024. [Online]. Available: https://betaflight.com/docs/wiki/app

[9] L. Su et al., "Real-time Guidance for Powered Landing of Reusable Rockets via Deep Reinforcement Learning," in 2022 IEEE ICUS, Oct. 2022, pp. 214–219. doi: 10.1109/ICUS55513.2022.9986540.

[10] G. J. Blaney and D. R. Holder, "Drag Coefficients for Cylinders at Subsonic Velocities," NASA Technical Note TN D-1540, 1963.

Appendix A: Python Analysis Code

A.1 Attitude PID Simulation: Part 1 Model, Equations G through J

The following Python code implements the numerical simulation of Equations G–J from Part 1. This code was used to generate the model prediction curves in Figure 5.

```
import numpy as np

def simulate_attitude(Kp=2.5, Ki=0.10, Kd=0.80, theta0_deg=10.0):
    """Simulate closed-loop attitude PID response (Equations G-J)."""
    Icm = 0.042    # moment of inertia about transverse axis (kg*m^2)
    rcm = 0.15     # gravitational lever arm (m)
    darm = 0.20    # pneumatic nozzle moment arm (m)
    m = 1.05       # total system mass (kg)
    g = 9.81       # gravitational acceleration (m/s^2)
    dt = 0.004     # integration time step (s)
    N = 750        # number of time steps (3.0 s total)

    theta = theta0_deg * np.pi / 180  # initial tilt (rad)
    theta_dot = 0.0                   # initial angular velocity (rad/s)
    integral = 0.0                    # integral term accumulator

    times, angles = [], []
    for i in range(N):
        e = -theta                    # error signal: e(t) = -theta(t)
        integral += e * dt            # Ki integral term
        tau_cmd = Kp*e + Ki*integral + Kd*(-theta_dot)  # Eq. I
        # Eq. J: full closed-loop dynamics
        alpha = (-m*g*rcm*theta + tau_cmd*darm) / Icm
        theta_dot += alpha * dt
        theta     += theta_dot * dt
        times.append(i * dt)
        angles.append(theta * 180 / np.pi)
    return np.array(times), np.array(angles)
```

A.2 Motor Spin-Up Fit: Equations D and E

The following code fits the measured RPM time history to the first-order model of Equation D using least-squares optimization.

```
from scipy.optimize import curve_fit

def spinup_model(t, omega_max, tau):
```

```
    """Equation D: first-order motor spin-up model."""
    return omega_max * (1 - np.exp(-t / tau))

def fit_spinup(t_measured, rpm_measured):
    """Fit measured RPM curve to Equation D."""
    popt, pcov = curve_fit(spinup_model, t_measured, rpm_measured,
                           p0=[18000, 0.25],   # initial guess
                           bounds=([5000, 0.01], [40000, 2.0]))
    omega_max_fit, tau_fit = popt
    return omega_max_fit, tau_fit

# Load from Betaflight blackbox CSV
# data = np.loadtxt("blackbox_export.csv", delimiter=",", skiprows=1)
# t_meas = data[:, 0] * 0.000125    # loopIteration * 125 us
# rpm_meas = data[:, eRPM_col] / 7  # eRPM / (pole_pairs) = mechanical RPM
# omega_fit, tau_fit = fit_spinup(t_meas, rpm_meas)
# print(f"tau_measured = {tau_fit:.4f} s")
```

A.3 Guidance Simulation: Equations K through N

The following code simulates the horizontal guidance PID loop for re-calibration Analysis 4.

```
def simulate_guidance(Kp_g=1.2, Kd_g=0.60, Fmax=4.0,
                      t_avail=10.3, x0=5.0, Ki_g=0.05):
    """Simulate horizontal guidance PID (Equations K-N)."""
    m = 1.05   # total mass (kg)
    b = 0.05   # horizontal aerodynamic drag coefficient
    dt = 0.04  # integration time step (s)
    N = int(t_avail / dt) + 1

    x, xdot, integral = x0, 0.0, 0.0
    times, positions = [0], [x0]
    for i in range(1, N):
        e = x                          # position error
        integral += e * dt             # integral accumulator
        # Eq. L: PID guidance force command
        Fcmd = -(Kp_g*e + Ki_g*integral + Kd_g*xdot)
        Fcmd = np.clip(Fcmd, -Fmax, Fmax)  # Eq. M: saturation
        xdot += ((Fcmd - b*xdot) / m) * dt  # Eq. K
        x += xdot * dt
        times.append(i * dt)
        positions.append(x)
    return np.array(times), np.array(positions)
```

Equation List:

[A] (Net Force/Newton's Second Law): This fundamental physics principle explains how force equals mass times acceleration (F=ma). Newton's Second Law of Motion

[B] & [C] (Terminal Velocity): These equations describe the point where drag and thrust balance gravity to reach a constant descent speed. Terminal Velocity Equation Explained

[D] (Motor Spin-up Time Constant): A guide on how mechanical time constants govern the speed response of DC motors. DC-Motor Calculations & Parameters

[E] (Thrust vs. RPM): This research highlights the quadratic relationship where thrust increases with the square of the rotational speed. Propeller Performance Curves

[F] (Aerodynamic Drag Torque): Technical analysis of the torque experienced by rotating bodies in a fluid. Aerodynamic Torque on a Rotating Disc

[G] (Euler's Rotational Equation): The standard equations used to describe the rotation of a rigid body. Euler's Equations for Rigid Body Dynamics

[H] (Small Angle Approximation): A mathematical tool used to simplify trigonometric functions for control models. Small Angle Approximations

[I] & [L] (PID Control Law): A detailed explanation of how proportional, integral, and derivative terms combine to manage error. PID Theory Explained

[J] (Closed-Loop Dynamics): Documentation on how feedback systems stabilize a process. Closed-Loop Control Techniques

[K] (Horizontal Motion with Drag): Mathematical modeling of projectiles or vehicles moving horizontally through air. Projectile Motion with Air Resistance

[M] (Thrust Saturation): While specific to hardware, the concept of saturation in control systems is summarized here. PID Controllers & Saturation

[N] (Descent Correction Window): An application of basic kinematics for objects falling with air drag. Projectile with Air Drag Dynamics